Measuring high field gradients of cobalt nanomagnets in a spin-mechanical setup

Felix Hahne,[1,2,a)] Teresa Klara Pfau,[1,2,a)] Liza Žaper,[3,a)] Lucio Stefan,[1,2] Thibault Capelle,[1,2] Andrea Ranfagni,[1,2] Martino Poggio,[3] and Albert Schliesser[1,2]

[1)]*Niels Bohr Institute, University of Copenhagen, Blegdamsvej 17, 2100, Copenhagen, Denmark*

[2)]*Center for Hybrid Quantum Networks, Niels Bohr Institute, University of Copenhagen, Blegdamsvej 17, 2100, Copenhagen, Denmark*

[3)]*Department of Physics, University of Basel, Klingelbergstrasse 82, 4056 Basel, Switzerland*

(Dated: 27 August 2025)

Hybrid systems composed of a single nitrogen-vacancy center spin magnetically coupled to a macroscopic mechanical resonator constitute promising platforms for the realization of quantum information protocols and for quantum sensing applications. The magnetic structure that mediates the interaction must ensure high field gradients while preserving the spin and mechanical properties. We present a spin-mechanical setup built around a cobalt nanomagnet grown with focused electron beam-induced deposition. The magnetic structure is fully characterized, and a maximum gradient of $170\,\mathrm{kT\,m^{-1}}$ is directly measured at a spin-oscillator distance of a few hundred nanometers. Spin coherence was preserved at the value of $20\,\mu\mathrm{s}$ up to a gradient of $25\,\mathrm{kT\,m^{-1}}$. The effect of the mechanical motion onto the spin dynamics was observed, thus signifying the presence of spin-mechanics coupling. Given the noninvasive nature of the nanomagnet deposition process, we foresee the adoption of such structures in hybrid platforms with high-quality factor resonators, in the "magnet on oscillator" configuration.

[a)]These authors contributed equally to this work.

Following the landmark experiment[1] that revealed how a single electron spin can exert a measurable force on a macroscopic cantilever, various hybrid platforms composed of two-level systems coupled to macroscopic oscillators have emerged by integrating mechanical resonators with superconducting qubits[2–5] and solid state defects[6,7]. Thanks to the mature technology of ultra-high quality factor oscillators[8], these platforms are appealing as testbeds for quantum information processing experiments[9] and also for pushing the boundaries of quantum sensing[10].

The paradigmatic system of a single spin coupled to a mechanical resonator device has been successfully implemented using NV defects in diamond[11] coupled to the mechanics via strain[12,13] or magnetically[14–20].

When a magnetically-decorated oscillator is placed in the vicinity of an NV center[21], the Zeeman interaction results in a parametric single-phonon coupling strength $g_0 = 2\pi\gamma_{\rm NV} G_{\rm z} z_{\rm zpf}$, where $\gamma_{\rm NV} \simeq 28\,{\rm GHz\,T^{-1}}$ is the gyromagnetic ratio of the NV center, $G_{\rm z} = \partial B_{\rm NV}/\partial z$ is the gradient at the NV rest position—along the oscillator's motion direction (z)—of the magnetic field component ($B_{\rm NV}$) parallel to the NV spin quantization axis, and $z_{\rm zpf} = \sqrt{\hbar/2m\Omega_{\rm m}}$ is the zero-point motion amplitude, where $\hbar$ is the reduced Planck constant, $\Omega_{\rm m}$ is the oscillator's angular frequency, and m is its mass.

A crucial requirement for implementing quantum protocols is achieving a quantum cooperativity greater than one, with the cooperativity defined[15] as $C = g_0^2 T_2 \Gamma^{-1}$, where Γ in the decoherence rate of the oscillator, and T_2 denotes the spin transverse relaxation time under a specific decoupling sequence. When $C > 1$, the zero-point mechanical fluctuations could be resolved within a few shot measurements[15,22]. In this regime, a hot mechanical resonator could be exploited to realize quantum gates between two spins in a hybrid nano-electromechanical system[23], or – when $C > 4$ – to efficiently generate entanglement between two spin qubits[24].

An important challenge currently faced by the community in this regard, is the research of a suitable magnetic structure, which must achieve high magnetic field gradients while preserving both the oscillator's properties and the overall system coherence[25]. Different methods have been explored, including the use of NdFeB magnetic structures[14], a CoFe magnetic film evaporated onto a quartz tip[19], a CoCr layer deposited on a tip[15], and NdFeB beads[16,18].

Here, we harness the nanometric control of focused electron beam induced deposition (FEBID)[26] to grow soft cobalt nanomagnets on a silicon chip. The nanomagnetic structure, which exhibits strong magnetic gradients, is installed in a spin-mechanics setup based on a scanning NV microscopy configuration.

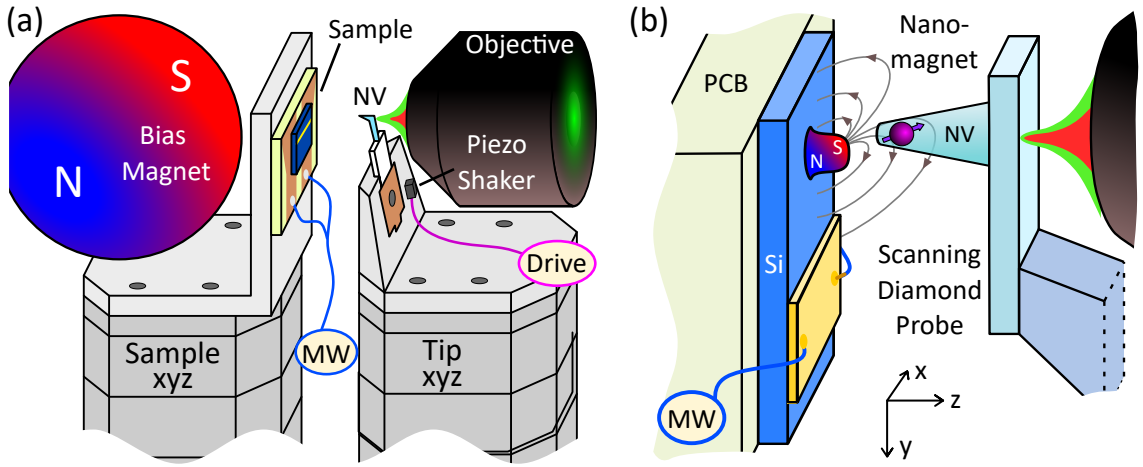

FIG. 1. Schematic of the scanning setup. (a) Sample and NV probe are mounted on two x,y,z piezo scanners. The nanomagnets are magnetized by a 4 cm-diameter spherical permanent magnet at a distance of a few millimeters. A 0.9 NA and 1 mm working distance objective focuses the collimated excitation beam onto the NV attached to a quartz tuning fork. A piezo shaker mechanically excites the tuning fork motion. (b) Depicted is a single nanomagnet in proximity of the microwave (MW) stripline and the NV probe in the laboratory frame. The silicon chip is placed in the apparatus with a printed circuit board holder that also provides the microwave contacts.

The scanning NV microscopy configuration we use for this work utilizes x,y,z piezoelectric nanopositioners (attocube), allowing nanometer-resolution spatial positioning of the mounted tuning fork with the NV center relative to a selected sample with the nanomagnets (Fig. 1(a)). The nanomagnets are magnetized by a homogeneous external magnetic bias field of up to 140 mT generated by a spherical magnet which is aligned to the NV quantization axis. Excitation with laser light at a wavelength of 515 nm and readout of the NV photoluminescence rate are carried out using a home-built confocal microscope with a 0.9 NA objective (Olympus MPlanFL N 100x). The scanning system is configured vertically to allow the insertion of a permanent magnet for magnetic biasing on the backside of the sample chip.

The core of the system consists of a 100-cut diamond scanning probe (QZabre QST[27]), hosting the NV center, and a Si chip with the Co nanomagnets plus an integrated microwave stripline for spin control (Fig. 1(b)). The nanomagnet of this study is approximately 40 µm away from the stripline and has a cylindrical shape with 830 nm height and 400 nm diameter.

To grow these nanomagnets we employ FEBID with the geometry defined as a circular pattern

and the following parameters: an acceleration voltage of 5 kV, a beam current of 100 pA, a dwell time of 1 µs, and a precursor flux corresponding to a vacuum pressure varying in the range 1.1×10^{-6} mbar to 1.2×10^{-6} mbar (see SI Appendix A 2).

We perform magnetometry measurements[28–30] to characterize the stray field $\mathbf{B}_{\mathrm{nm}}(x,y,z)$ emanating from the nanomagnet. We measure the shift in the lower energy electron spin resonance of the optical ground state spin triplet while performing a *xy* raster scans on planes above the magnetic structure. The optically detected magnetic resonance (ODMR) is performed at each position (x,y) by applying a continuous-wave microwave sweep and acquiring the NV center photoluminescence rate[31]. The scans are performed on a single nanomagnet under ambient conditions, without feedback and hovering at a fixed height above the substrate. The spin resonance frequencies $\nu_{\mathrm{res}}^{\pm}$, in the relevant experimental configuration, reads:

$$\nu_{\mathrm{res}}^{\pm} \simeq |\nu_0 \pm \gamma_{\mathrm{NV}} B_{\mathrm{NV}}| \,. \tag{1}$$

Here, $\nu_0 \simeq 2.87$ GHz is the ground state zero-field splitting parameter and the total magnetic field is defined as $B_{\mathrm{NV}} = \mathbf{B}_{\mathrm{nm}} \cdot \hat{\mathbf{n}}_{\mathrm{NV}} + B_{\mathrm{bias}}$, where $\hat{\mathbf{n}}_{\mathrm{NV}}$ is the spin quantization axis direction, and the bias field is assumed to be aligned to the spin axis. We are neglecting the local off-axis strain field contribution to the energy levels, and we assume to operate the system in the regime where $B_{\perp} \ll |\nu_0/\gamma_{\mathrm{NV}} - |B_{\mathrm{NV}}||$, where $B_{\perp}$ is the magnitude of the field component orthogonal to the spin quantization axis. All acquired scanned maps display stray field patterns consistent with a magnetic dipole field as confirmed by dipole model fits shown in Fig. 2(a).

Approximating the nanomagnet as a dipole, we can extract the magnitude of the magnetic dipole moment m_{dip} from the dipole model fits (see SI Appendix B). We acquire a set of four scanned maps at different scanning heights to capture the stray field distribution at multiple distances from the nanomagnet. We increment the heights from 960 nm to 1460 nm above the nanomagnet in steps of $z_{\mathrm{step}} = 166(5)$ nm. The maps of a set share the same experimental conditions otherwise. A simultaneous fit across all four scanned maps as shown in Fig. 2(b), incorporating the known height steps z_{step}, additionally constrains the fit parameters $r_{\mathrm{z,0}}$ (depth of the approximated point-like dipole within the nanomagnet) and m_{dip}, which for individual maps can float in a correlated manner. The fit then allows quantitative inference of the magnetic moment magnitude m_{dip}. We repeat this fit procedure for external bias fields B_{bias} between from 30 mT to 140 mT and plot $m_{\mathrm{dip}}(B_{\mathrm{bias}})$ in Fig. 2(c,d) (green stars). The estimated dipole moment magnitude $m_{\mathrm{dip}}(B_{\mathrm{bias}})$ increases linearly, indicating a soft magnetic nature of the FEBID grown nanomagnet as expected

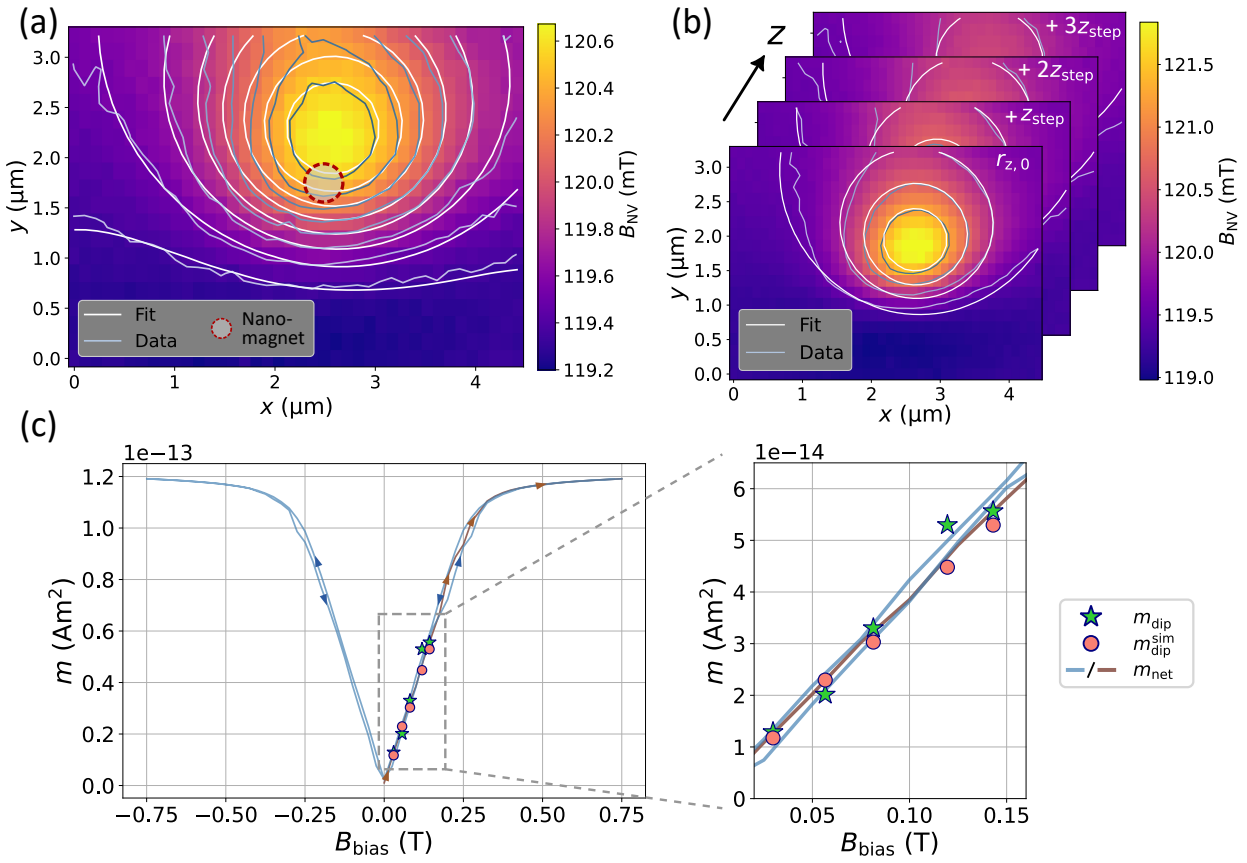

FIG. 2. Dipole fitting and stray field characterization. (a) A map of the measured B_{NV} at an estimated height of $h = 1294(40)\,\mathrm{nm}$ above the nanomagnet and with $B_{\mathrm{bias}} \sim 120\,\mathrm{mT}$. The white contour lines from a dipole model fit agree with the gray data contour lines of equal value. The indicated nanomagnet is centered around the dipole (x, y) position. (b) Simultaneous dipole fitting of four stray-field maps acquired at successive heights above the sample in increments of $z_{\mathrm{step}} = 166(5)\,\mathrm{nm}$. A global dipole depth $r_{\mathrm{z,0}}$ is enforced across all maps, while the relative height offset is fixed by the known step size. (c) Plot of the fitted dipole magnetic moment m_{dip} (green stars), dipole fitted $m_{\mathrm{dip}}^{\mathrm{sim}}$ (red dots) and simulated net magnetization m_{net} (blue and brown lines) with increasing external biasing field. For the hysteresis curve of m_{net} the external field is varied from $0\,\mathrm{mT} \rightarrow 750\,\mathrm{mT} \rightarrow -750\,\mathrm{mT} \rightarrow 750\,\mathrm{mT}$ in increments of $25\,\mathrm{mT}$. The brown line marks the initial upsweep from $0\,\mathrm{mT}$ to $750\,\mathrm{mT}$, while the blue line corresponds to the remainder of the sweep. Arrows on the lines indicate the sweep direction of the external field. The inset displays a zoomed-in section of the boxed data region for improved visibility of the individual points.

from their typically amorphous structure[32].

For comparison, we similarly perform the simultaneous fits on stray field maps generated by

a simulation of the nanomagnet, that is based on the dipole fit and AFM topography (see SI Appendix C), extracting $m_{\mathrm{dip}}^{\mathrm{sim}}(B_{\mathrm{bias}})$ (red circles in Fig. 2(c,d)) that agrees well with $m_{\mathrm{dip}}(B_{\mathrm{bias}})$. Furthermore, we can calculate the net magnetic moment magnitude of the simulated nanomagnet via the volume integral of the magnetization $m_{\mathrm{net}} \approx |\sum_{ijk} \mathbf{M}_{ijk} \Delta V|$, where $\mathbf{M}_{ijk}$ is the magnetization in each simulation cell of volume ΔV. The moment magnitude $m_{\mathrm{net}}(B_{\mathrm{bias}})$ is depicted in Fig. 2(c,d). The agreement between m_{dip}, $m_{\mathrm{dip}}^{\mathrm{sim}}$, and m_{net} demonstrates mutual validation across of the experimental measurements, the dipole model fit, and the simulation.

The simulation of the magnetic structure predicts that the nanomagnet—that is $m_{\mathrm{dip}}(B_{\mathrm{bias}})$—approaches saturation[33] at around $B_{\mathrm{bias}} \sim 300\,\mathrm{mT}$. Supporting this prediction we find agreement between the ratio of the bias fields $140\,\mathrm{mT}/300\,\mathrm{mT} = 0.47$ and the magnetization ratio $M/M_{\mathrm{sat}} = 0.45$, where $M = m_{\mathrm{dip}}(B_{\mathrm{bias}} = 140\,\mathrm{mT})/V$ with the nanomagnet volume V and saturation magnetization $M_{\mathrm{sat}} = 1.26\,\mathrm{MA\,m^{-1}}$ used for the simulation[34].

Foreseeing a future implementation of the experiment in which the magnetic structure is deposited on a high-Q resonator[35], enabling coupling between the out-of-plane motion and the NV center, we are interested in a direct measurement of the magnetic gradient along the z axis.

Under the applied B_{bias} we measured the gradient G_{z} directly by the Zeeman shift from ODMR spectra as the NV center was scanned through the stray field near the nanomagnet. Guided by both the dipole model fit and the simulation, we identified the region of highest projected field gradient G_{z}, while minimizing magnetic field $B_{\perp}$ that is transverse to $\hat{\mathbf{n}}_{\mathrm{NV}}$, ensuring that the conditions of the Eq. (1) remains valid.

As shown in Fig. 3(a-c) we find this region—which is governed by the relative angles between NV and magnetic dipole orientation—towards the edge of the nanomagnet. There, we approached the nanomagnet in the z direction and acquired ODMR spectra of the lower energy spin resonance at multiple positions to extract the projected magnetic field $B_{\mathrm{NV}}(z)$ as a function of distance to the nanomagnet surface Δz.

In Fig. 3(d), we present the measured stray fields $B_{\mathrm{NV}}(z)$ for the two approach trajectories exhibiting the highest field gradients, recorded at a bias field $B_{\mathrm{bias}} \sim 120\,\mathrm{mT}$. The corresponding field gradients $G_{\mathrm{z}}(z)$ are shown in Fig. 3(e), with maximum measured values of $B_{\mathrm{NV}} = 40\,\mathrm{mT} + B_{\mathrm{bias}}$ and $G_{\mathrm{z}} = 170\,\mathrm{kT\,m^{-1}}$ obtained $\sim 250\,\mathrm{nm}$ above the nanomagnet. Acquiring ODMR spectra closer to the surface is hindered by the reduced ODMR signal contrast, which lowers the signal-to-noise ratio below unity (see SI Appendix D). We attribute this to mechanical drifts in the setup in the high-gradient field, primarily caused by microwave-induced heating.

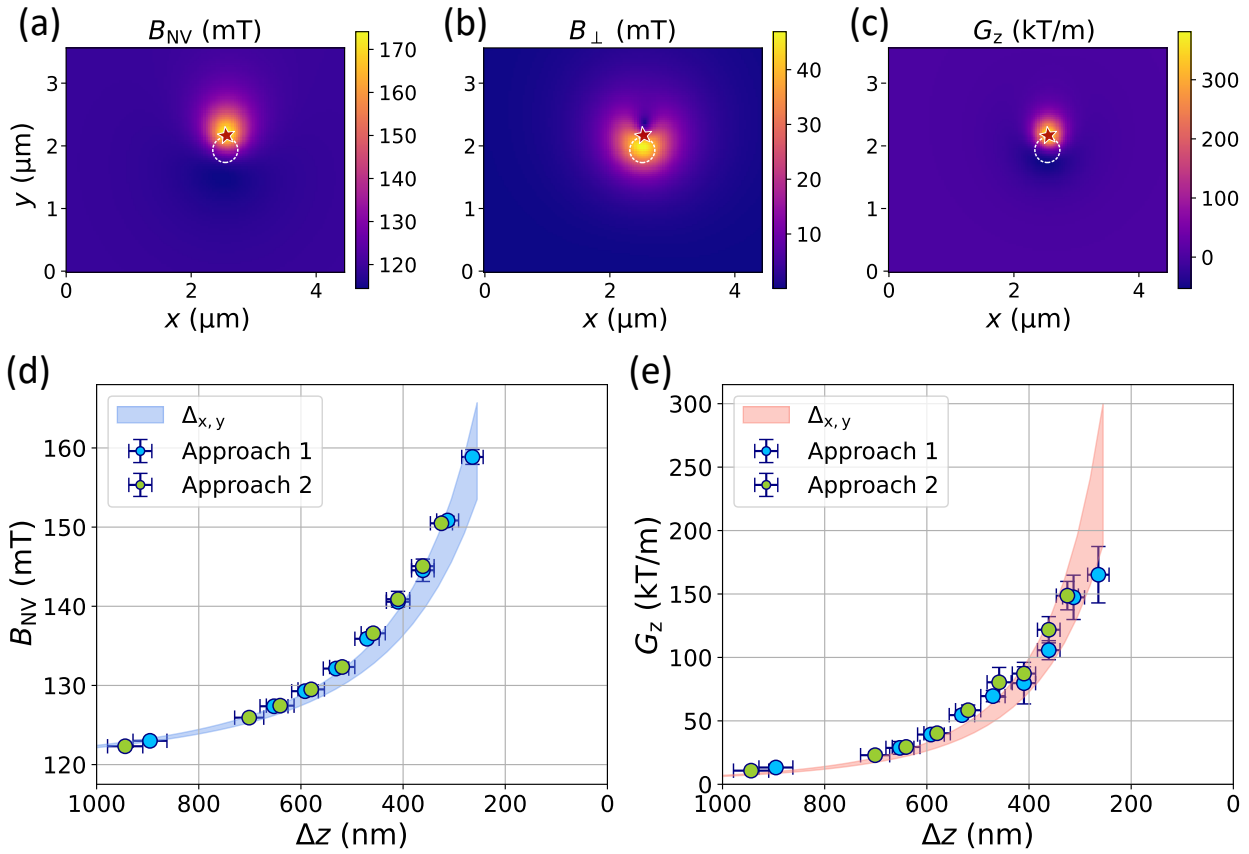

FIG. 3. Optimal approach region from simulations for measurement of the vertical gradient. (a-c) Simulation maps of B_{NV}, $B_\perp$ and G_z with the same x,y-axes as Fig. 2(a), but at a height $h = 200\,\mathrm{nm}$ above the nanomagnet. The white dotted circles mark the position and width of the simulated nanomagnet, the red star highlight the approach location. (d) Plots of the measured magnetic field $B_{\mathrm{NV}}(z) + B_{\mathrm{bias}}$ and (e) the gradient $G_z(z)$ from two approaches as a function of the distance to the nanomagnet Δz. The zero points on the abscissa mark the AFM contact with the surface which was measured before each approach. $\Delta_x = 111\,\mathrm{nm}$ and $\Delta_y = 108\,\mathrm{nm}$ correspond to the width of the vertically approached region. A description of the error bars are in SI Appendix D.

After characterizing the DC behavior of the spin-mechanical system, we study the dynamics of the NV center using coherent spin control. We measured the spin decay time under spin-echo sequence, $T_{2\mathrm{E}}$, while the NV probe was positioned above the nanomagnet (Fig. 4(a)). The π-pulse time was first characterized with a Rabi measurement, from which we extract the π-pulse durations of $\sim 55\,\mathrm{ns}$. The spin-echo scheme shown in the inset of Fig. 4(a) was applied in two different variations, where the rotation axis of the final $\pi/2$-pulse is either along the X or the $-X$ axis as defined in the Bloch sphere in the inset of Fig. 4(b). Defining I_X and I_{-X} as the measured

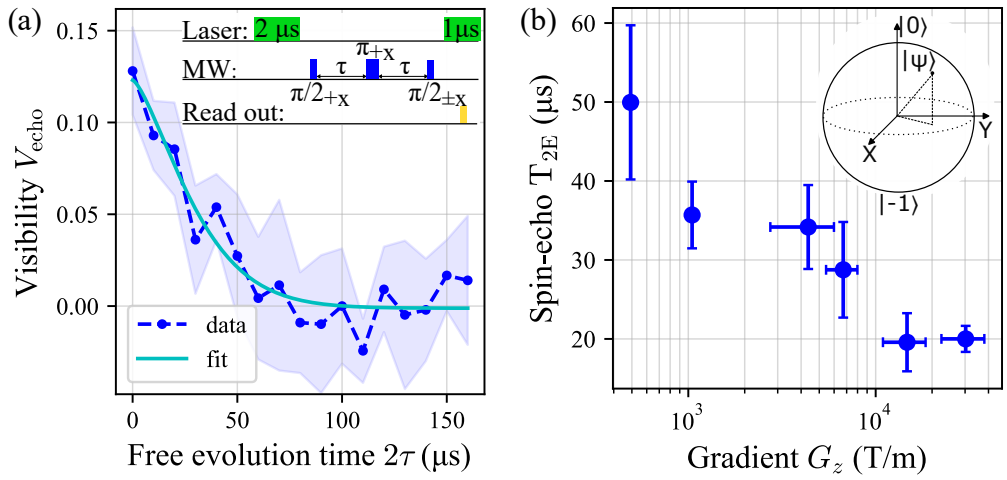

FIG. 4. Controlling the NV center's spin in a gradient field. (a) T_{2E} measurement in the gradient field of the nanomagnet. The inset shows the used pulse scheme. Visibility is calculated following[36] from two separate spin echo measurements where the last $\pi/2$ pulse is either applied along the $+X$ or $-X$ axis. This measurement was done at $G_z = 4.4(1.6)\,\mathrm{kT\,m^{-1}}$ and gives $T_{2E} = 34.0(5.3)\,\mu\mathrm{s}$. The shaded area shows the standard deviation. (b) Multiple T_{2E} measurements at different positions in the gradient field G_z of a nanomagnet. The measurements were done at distances between approximately 1587 nm and 540 nm. The Bloch sphere in the inset defines the axis of the rotation.

photoluminescence rate at the end of a spin-echo sequence for the two readout configurations, we compute the visibility $V_{\mathrm{echo}} = (I_X - I_{-X})/(I_X + I_{-X})$, which rejects the common-mode noise[36]. The visibility V_{echo} is then fitted with an exponential decay to extract T_{2E}. This measurement was repeated at different positions in the gradient field G_z. In Fig. 4(b) the dependency of T_{2E} on G_z is shown. The shift due to instabilities during T_{2E} measurements are indicated by horizontal error-bars. Applying a MW drive in the vicinity of the NV and the nanomagnet causes heating leading to a shift of ODMR resonance. Therefore it is not possible to apply accurate on-resonance pulses at gradients higher than $30\,\mathrm{kT/m}$. The vertical error-bars are extracted from the fit of T_{2E}.

Starting from a value $T_{2E} = 56(6)\,\mu\mathrm{s}$ for a measurement far away from the nanomagnet, T_{2E} in Fig. 4(b) shows a significant decrease in value towards higher gradients. This trend can be attributed to either magnetic field noise from the magnetic nano-structure, or thermal drifts of the system, which translates into fluctuations in the frequency of the NV center causing dephasing[25].

To show that the presented setup is suitable for performing a spin-mechanical experiment, we further measure the effect of the tuning fork mechanical oscillation on the spin dynamics. As the

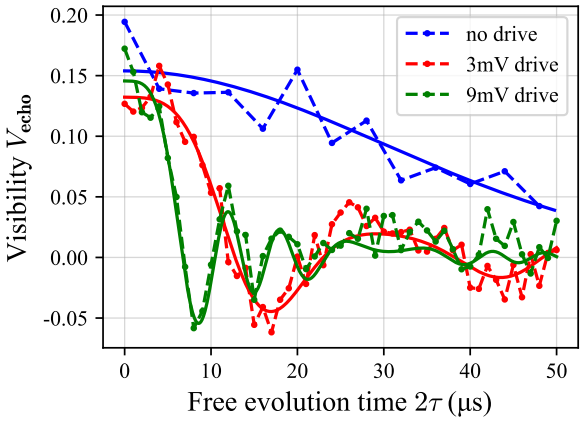

FIG. 5. Impact of mechanical oscillation of the tuning fork on the NV center. Blue curve shows a spin-echo measurement for an undriven tuning fork. The red and green curves show the measurement with a driven tuning fork at $\Omega_{\mathrm{m}} \approx 32\,\mathrm{kHz}$ with 3 mV and 9 mV driving amplitude, receptively. Data (dotted lines) can be fitted with a Bessel function of 0th order (full line).

tuning fork is driven at its resonance frequency and vibrates along the x direction, we measure a series of unsynchronized spin-echo sequences (Fig. 5) with the NV center moving in a gradient $G_x = \partial B_{\mathrm{NV}}/\partial x \simeq 540\,\mathrm{T\,m^{-1}}$.

When the tuning fork is not driven, we see undisturbed decay of the visibility with a $T_{2\mathrm{E}} = 42(3)\,\mu\mathrm{s}$ (blue curve). In contrast to that, a driven tuning fork results in a modulated decay (red and green curves). It can be fitted to a zeroth order Bessel function,[18]

$$V_{\mathrm{echo}} = \frac{C J_0\left(\frac{4\pi\gamma_{\mathrm{NV}} x_0 G_x}{\Omega_{\mathbf{m}}}(\cos(\Omega_{\mathrm{m}}\tau)-1)\right)}{2-C} \exp\left[-\left(\frac{2\tau}{T_{2\mathrm{E}}}\right)^n\right], \tag{2}$$

clearly indicating spin mechanical coupling, where C is the contrast of our measurement and x_0 is the motional amplitude of the NV center (see SI Appendix E).

The oscillation amplitude values extracted from the fit are $x_0 = 3(1)\,\mathrm{nm}$ (red curve) for a piezo drive amplitude of the tuning fork of 3 mV, and $x_0 = 11(1)\,\mathrm{nm}$ (green curve) for a drive amplitude of 9 mV. In the two configurations, the mechanical motion maps into an oscillating magnetic field with amplitude $2.0(6)\,\mu\mathrm{T}$ and $6.1(8)\,\mu\mathrm{T}$ at the position of the NV center, respectively.

In conclusion, we have demonstrated the generation of strong magnetic field gradients—up to $170\,\mathrm{kT\,m^{-1}}$—using a soft cobalt nanostructure integrated into a spin-mechanics platform based on

a scanning NV microscopy configuration. Spin coherence measurements performed in magnetic field gradients up to $25\,\mathrm{kT\,m^{-1}}$ revealed a coherence time $T_{2\mathrm{E}}$ of at least $20\,\mu\mathrm{s}$. Considering that the experiments were conducted under open-loop mechanical conditions, we expect that, with cryogenic operation and active stabilization, spin manipulation at even higher field gradients could be achievable. Moreover, we observed a clear influence of the tuning fork motion on the NV spin coherence, indicating the presence of measurable spin-mechanical coupling in our setup.

Crucially, the non-invasive nature of the nanomagnet deposition via FEBID allowed us to successfully decorate a silicon nitride membrane[37] with the magnetic structure (see SI Appendix A 2). This opens the path for further studies, including the investigation of potential changes in the mechanical quality factor resulting from the deposition—an essential step for future quantum spin-mechanics applications. If the membranes degradation is negligible, and we consider a typical resonance frequency of 1.5 MHz, an effective mass of 2 ng and an ultra-high quality factor[38] $Q = 10^9$ at 4 K, then with a spin coherence time of 1 ms and a magnetic gradient of $170\,\mathrm{kT\,m^{-1}}$ we obtain a single-phonon coupling strength $g_0/2\pi = 8\,\mathrm{Hz}$. This corresponds to a cooperativity $C = 5\times10^{-3}$, which is four orders magnitude higher than current state-of-the-art setups[18]. Remarkably, the force sensitivity of such a device—limited by the thermal contribution $S_{\mathrm{th}} = 4k_{\mathrm{B}}Tm\Omega/Q = 4\,\mathrm{aN^2/Hz}$ (with k_{B} the Boltzmann constant)—would be comparable to the amplitude of the force produced by the oscillating spin $F = \mu_{\mathrm{B}}G = 1.6\,\mathrm{aN}$, thus making it possible to detect the force exerted by the single spin within a few seconds averaging time, during which the spin can be re-polarized as necessary.

Reaching the milestone of $C \sim 1$ requires technical advances, and appears feasible with the optimistic value[36] of $T_2 = 10\,\mathrm{ms}$, and a gradient of $1\,\mathrm{MT\,m^{-1}}$, predicted at a feasible distance of 150 nm from the magnetic structure at saturation.

Furthermore, the demonstrated ability to grow nanomagnets directly on membranes provides a promising platform for implementing quantum sensing experiments. While membranes have recently been integrated into scanning force microscopy setups[39,40] and adopted in sample-on-resonator configurations for magnetic resonance force detection[41], we foresee their use in magnetic resonance force microscopy experiments in the practical "magnet-on-resonator" configuration[42], as well as for advancing nanoscale magnetic resonance imaging techniques[10].

Finally, the high degree of control offered by the FEBID technique enables the tailoring of nanomagnet geometry to suit specific experimental requirements of the magnetic field, making it a versatile tool for future developments in hybrid quantum systems.

Appendix A: Experimental Setup

1. Microwave Antenna Fabrication

Microwave striplines for the experiments are fabricated on high-resistivity ($>20\,000\,\Omega\,\mathrm{cm}$) 4-inch silicon wafers, polished on one side and $500(25)\,\mu\mathrm{m}$ thick. A $>1.5\,\mu\mathrm{m}$ layer of AZ 701 MIR photoresist is spin-coated, soft-baked, exposed with a maskless aligner, post-baked, and developed in TMAH. After surface cleaning with an ion gun in an electron beam evaporator, a 5 nm chromium adhesion layer and 100 nm gold layer are deposited. Lift-off is performed in 1165 remover, followed by cleaning in IPA, deionized water, and spin drying. To protect the structures, another photoresist layer is applied and baked and the wafer is diced with a diamond saw. Individual chips are cleaned in acetone and IPA and wirebonded to the printed circuit board before use.

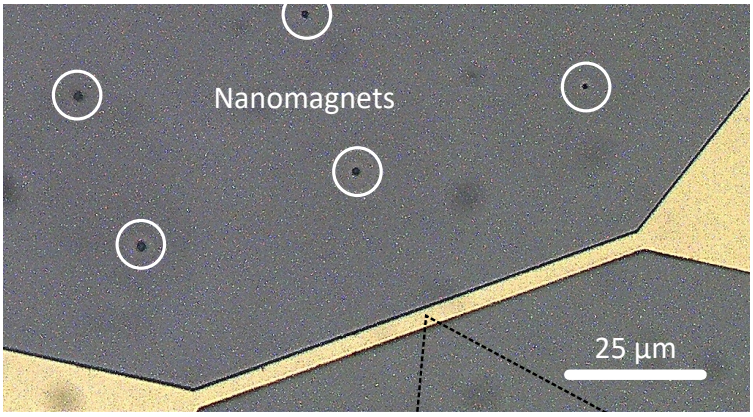

FIG. 6. Micrograph of the tapered down region of the MW stripline. Individual nanomagnets are deposited near the stripline as highlighted.

2. FEBID Growth of Nanomagnet

The nanomagnets are positioned at distances ranging from 30 µm to 210 µm from the stripline and are laterally separated from each other by 60 µm in a grid pattern—sufficient to prevent mutual interaction via stray fields. The deposition starts by releasing the precursor molecule $Co_2(CO)_8$ in the vacuum chamber through a gas injection system (GIS, see Fig. 7). The desired geometry is defined as a circular pattern in the computer-aided interface, where the irradiated precursor molecule adsorbs on the surface as the focused electron beam follows the circular raster pattern from the

center outward. Initially, we deposited arrays of 4 by 4 circular geometry nanomagnets with defined pattern diameters and heights: 250 nm, 200 nm, 150 nm, 100 nm and 50 nm. With the goal in mind to deposit Co nanomagnets on thin, insulating SiN membranes, which exhibit high charging when exposed to an electron beam[43], we opt for the following FEBID parameters: acceleration voltage of 5 kV, beam current of 100 pA, dwell time of 1 μs, and precursor flux corresponding to a vacuum pressure varying in the range of $(1.72 - 2.78) \times 10^{-6}$ mbar. We note the deposited structures show a systematic offset from the defined deposit diameter, ranging between 20 nm and 100 nm. The offset may come from the charging effect which is commonly referred to as the halo, and it is produced through a dissociation of the adsorbed precursor by a cascade of secondary electrons generated through backscattering of electrons off the substrate and the grown deposit[34,44]. Further, we note that the defined pattern influences the charging effect. In a circularly defined pattern the beam irradiation time per area is maximum in the center of the structure, causing higher charging over time, while for a raster-scanned rectangular pattern the deposition is more uniform. For our purpose of growing test nanomagnets on silicon chip this effect is seen as an increase in the diameter. Conversely, in the growth of nanomagnets on silicon membranes (Fig. 8), where the substrate is an insulating material SiN, and has a thickness of 50 nm, we used a rectangular pattern that combined with the scattering of electrons at the edges results in a circular-shaped structure.

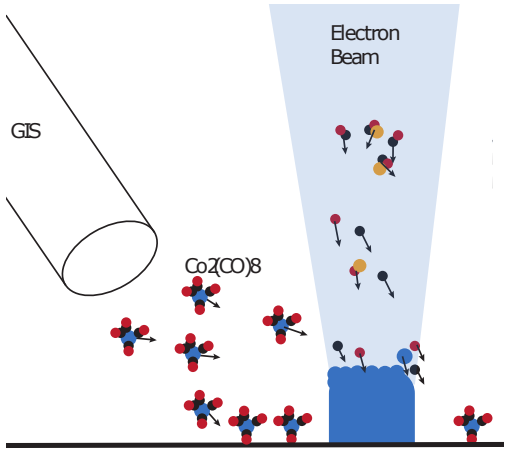

FIG. 7. Schematic of a FEBID process where a rectangular beam pattern is employed to create a structure from precursor molecules injected by the gas injection system (GIS).

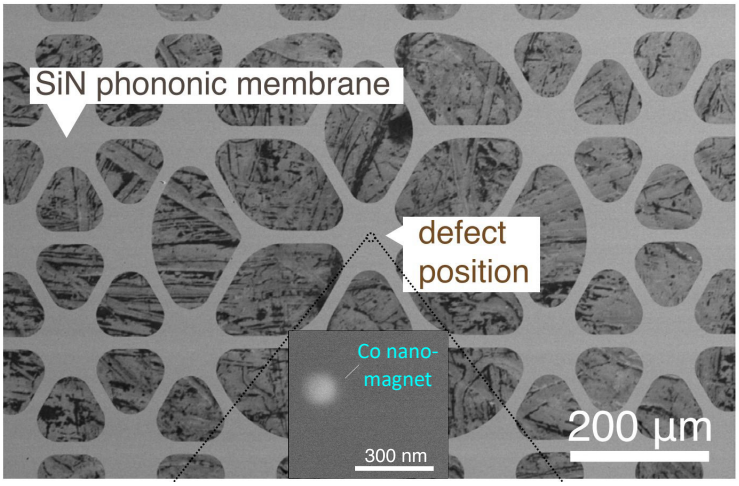

FIG. 8. (a) Top view of a SiN membrane, indicating the position of deposited area. Inset: an SEM image of a Co nanomagnet grown on a SiN membrane using a rectangular beam pattern, resulting in a circular-shape structure with a diameter of 100 nm.

3. External Bias Field

A 4 cm diameter spherical NdFeB magnet (Supermagnete, K-40-C) with $B_r = 1.26\,\mathrm{T}$ to $1.29\,\mathrm{T}$ residual field density is used. The magnet is inserted into a 3D printed cage which secures it in place while allowing manual rotation. Combined with translation stages, a rotator and a goniometer, the magnet can be freely aligned. The alignment is performed by centering the frequency splitting of the spin resonances $\nu_{\mathrm{res}}^{\pm}$ from Eq. (1) symmetrically around ν_0. According to[45] we calculate the norm $|\nabla B_{\mathrm{bias}}(r,\theta)| \simeq 10\,\mathrm{T/m}$ of the magnetic field produced by a spherical permanent magnet at a distance $r(B_{\mathrm{bias}} = 120\,\mathrm{mT}, \theta = 30^\circ)$ that matches the scanning plane position. A Comsol simulation of such a permanent magnet verifies this estimation. With this at hand, the variation of ΔB_{bias} across the scanned map shown in Fig. 2 (a) is expected to be $30\,\mu\mathrm{T}$, which low compared variation of the nanomagnetic stray field of a couple of mT.

4. Characterization of the Nanopositioners

z - Characterization

Long-lasting PL oscillations are observable when moving the NV probes in the z direction in the vicinity ($\sim 5\,\mu\mathrm{m}$) to the sample surface, that correspond to fluctuations in the excitation of the

NV due to self-interference of the excitation laser with its back-reflection at the sample surface[46]. These fringes occur with the laser wavelength $\lambda_L = 515\,\mathrm{nm}$ and by comparing them with measured fringe period, we can estimate the voltage-to-distance ratio C_z of the z-scanner. Analyzing 47 PL traces with such oscillations, acquired equivalently with the same sample and NV probe over multiple weeks, we did not observe a systematic change in C_z over time that exceeds statistical fluctuations.

An angle α between the reflection plane and the normal plane (see Fig. 9(a)) increases the interference fringe spacing to

$$C_{z,\mathrm{gen}}(\alpha) = \frac{2C_z}{1+\cos(2\alpha)}\,. \tag{A1}$$

We probe the angle α by measuring individual AFM contact points on the sample. In a fixed-point numerical iteration we find the fixed points

$$C_{z,\mathrm{gen}} = 1214(39)\,\mathrm{nm/V}\,, \qquad \alpha = 19.42(24)^\circ\,. \tag{A2}$$

We verify $C_{z,\mathrm{gen}}$ by comparing the topographic heights of the nanomagnet measured with the presented scanning NV platform and with a commercial calibrated AFM (Bruker, Dimension Icon PT) and find good agreement using $C_{z,\mathrm{gen}}$ as the conversion factor for the scanner voltages. All shown z-scanning distances in the main text are obtained from $C_{z,\mathrm{gen}}$ including a NV depth inside the diamond probe apex of $d_{\mathrm{NV}} = 70(20)\,\mathrm{nm}$.

x,y - *Characterization*

We use a checker pattern grid (Anfatec, UMG01B) with well defined trench separations $(\Delta x_p, \Delta y_p)$ to characterize the x,y-scanning axes of the nanopositioner under the assumption that the two scanning axes are independent of each other. By measuring the voltage position $V_{x,p}$ of the pillars we can approximate the local piezo gain

$$g_x(V_x) = \frac{\mathrm{d}x}{\mathrm{d}V_x} \simeq \frac{\Delta x_p}{\Delta V_{x,p}}\,, \tag{A3}$$

by fitting a polynomial of second order to the measured distribution of pillar separations $\Delta x_p/\Delta V_{x,p}$. Integrating the piezo gain $g(V_x)$ in the scanned voltage region $[V_x^1, V_x^2]$ yields the actual scanned spatial distance Δx

$$\Delta x = \int_{V_x^1}^{V_x^2} g_x(V_x)\, dV_x\,. \tag{A4}$$

For the scanning y-axis, $g_y(V_y)$ and Δy are calculated analogously.

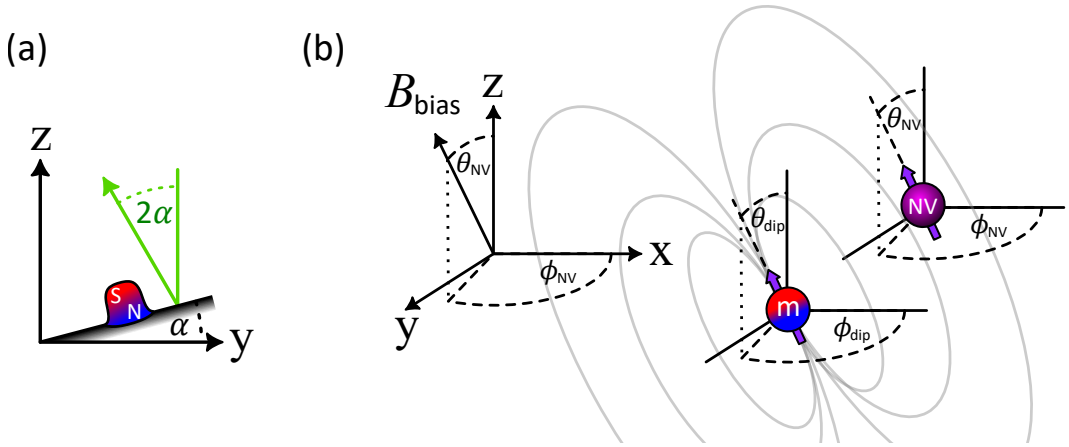

FIG. 9. Geometric overview. (a) Illustration of the sample tilt. Then green arrow is the back-reflected plane wave from the excitation laser (b) Summary of the NV and magnetic dipole angles.

Appendix B: Dipole Fit

Individual Dipole Fit

We use the model of a magnetic dipole $\mathbf{B}_{\text{dip}}$ projected on to the axis of the NV center $\hat{\mathbf{n}}_{\text{NV}}(\phi_{\text{NV}}, \theta_{\text{NV}})$,

$$\begin{aligned} B_{\text{NV}}(\mathbf{R}) &= \mathbf{B}_{\text{dip}}(\mathbf{R}) \cdot \hat{\mathbf{n}}_{\text{NV}} + B_{\text{bias}} \\ &= \frac{\mu_0}{4\pi} \left(\frac{3\mathbf{R}(\mathbf{m}_{\text{dip}} \cdot \mathbf{R})}{R^5} - \frac{\mathbf{m}_{\text{dip}}}{R^3} \right) \cdot \hat{\mathbf{n}}_{\text{NV}} + B_{\text{bias}} \,, \end{aligned} \tag{B1}$$

to fit the measured stray field of the nanomagnet in the main text (Fig. 2). We are scanning in planes at heights from 960 nm to 1460 nm above the nanomagnet. This includes the constant offset from the NV-to-sample distance which we measured independently in AFM contact to be 70(20) nm. We define the scanning plane as $\mathbf{R}(x,y) = (x - x_0, y - y_0, 0 - z_0)$, with dipole position (x_0, y_0, z_0), dipole magnetic moment $\mathbf{m}_{\text{dip}}$ and vacuum magnetic permeability μ_0. We approximate $\left(\hat{\mathbf{n}}_{\text{NV}}(\phi_{\text{NV}}, \theta_{\text{NV}}) \parallel \mathbf{m}_{\text{dip}}(\phi_{\text{dip}}, \theta_{\text{dip}})\right)$ (see Fig. 9(b)), which reduces the fit parameter space to $\{x_0, y_0, z_0, \phi_{\text{NV}}, \theta_{\text{NV}}, m_{\text{dip}}, B_{\text{bias}}\}$.

Simultaneous Dipole Fit

Incorporating the known height steps z_{step} in a simultaneous fit across the scanned maps of a set enforces consistency with the vertical decay trend of a dipolar field, $B_{\text{NV}} \propto m_{\text{dip}} / r_{\text{z},0}^3$, thereby

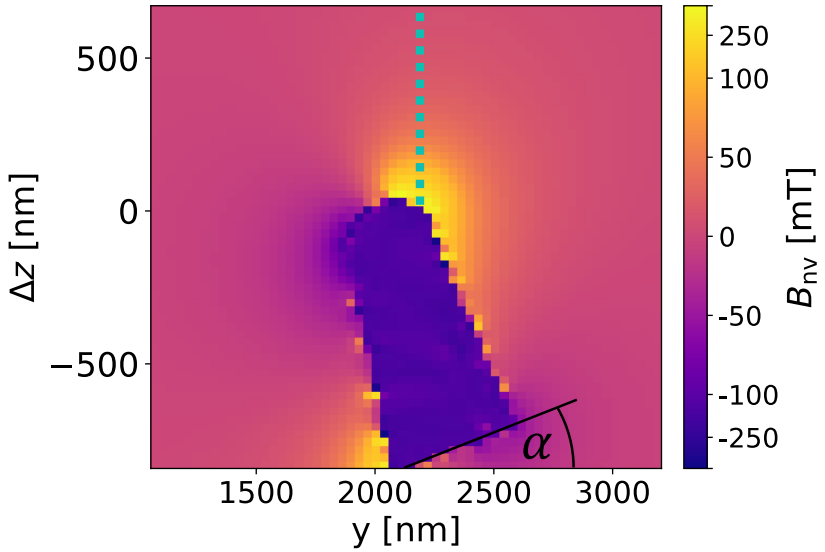

FIG. 10. Cross section of the simulated nanomagnet in the scanning frame scanning frame denoted in Fig. 1(b). The dashed line indicates the center of the approach region for the gradients measured in the main text with width $\Delta_{x,y}$. The angle α resembles the plane tilt. The colorbar is linear within $\pm 100\,\mathrm{mT}$ and logarithmic beyond that.

naturally constraining the strongly correlated $r_{z,0}$ and the magnetic moment m_{dip} parameters. The individual scanned maps can spatially vary in the xy-plane from each other. Pre-computation of the x_0, y_0 dipole positions of each map with the individual dipole fit allows further constrains. The global fit parameter space is then reduced to a $\{z_0, \phi_{NV}, \theta_{NV}, m_{dip}, B_{bias}\}$.

Appendix C: Micromagnetic Simulation of the Nanomagnet

We use the finite-difference micromagnetic simulation software MuMax3[47,48] to simulate the stray field of the FEBID grown nanomagnet using the parameters reported in[34,49]: exchange stiffness constant $A_{ex} = 14 \times 10^{-12}\,\mathrm{J\,m^{-1}}$, zero magnetocrystalline anisotropy and a saturation magnetization $M_{sat} = 1.26\,\mathrm{A\,m^{-1}}$ which is 90 % of the bulk value based on comparable literature on non-annealed structures[26,34].

The geometry of the simulated nanomagnet is based on the AFM topography acquired with a commercial AFM (Bruker, Dimension Icon PT). The simulation voxel size is $(36.83, 30, 25)\,\mathrm{nm}$ with a grid size of $(120, 100, 110)$ cells. We include an external bias field parallel to $\hat{\mathbf{n}}_{NV}$ with angles given by the dipole fit Fig. 2 (a) from the main text. To match the sample plane tilt α

from Appendix A 4, we rotate the nanomagnet accordingly. A cross section of the simulated nanomagnet is shown in Fig. 10. In the hysteresis the external bias field is varied from 0 mT $\rightarrow$ 750 mT $\rightarrow -750$ mT $\rightarrow$ 750 mT in increments of 25 mT.

Appendix D: Gradient Measurement

To estimate the stray field B_{NV} we use a Lorentzian model[28] to evaluate the ODMR spectra. As mentioned in the main text, every data point in Fig. 3 is evaluated from the average spectrum of three ODMR spectra taken consecutively. A first Lorentzian fit is used to define an ODMR window as twice the FWHM around the center frequency ν_0 of the ODMR dip. We assume gaussian noise as our base noise and calculate the standard deviation $\sigma = k_{\mathrm{gauss}} \cdot \mathrm{MAD}$ of the PL outside the defined ODMR window, where MAD is the median absolute deviation and k_{gauss} a scale factor for normally distributed noise. We have observed that our data acquisition card (National Instruments X Series) can induce single data point spikes in the measured PL. We attribute these outliers to a buffer overflow of the card. To exclude these outliers in a second fitting step, data points inside as well as outside the window that deviate by more than $3\,\sigma$ to the first Lorentzian fit are excluded. From the outlier-free second Lorentzian fit we estimate stray field of the nanomagnet via Eq. (1). Only ODMR measurements are considered that fulfill the two conditions:

- The frequency window of the full spectrum $\Delta\nu > 4\Gamma$.
- The ODMR contrast $C > 1\,\sigma$.

We argue that the first condition ensures to have enough statistical data to estimate a tangible MAD and to differentiate the ODMR signal from slow PL drifts. The second condition ensures SNR > 1. We give Γ as a conservative uncertainty for the stray field estimation ΔB_{NV}. The data acquisition time was set to 47 ms per MHz bandwidth resulting in a 10 s to 20 s of continuous wave MW emission for each data point - depending on the frequency range of the ODMR spectrum.

To probe and locate the region for the approaches shown in Fig. 3(d,e), we vertically approach the surface along the indicated line in Fig. 10 using the nanopositioners while monitoring the PL.

Error Bars

The gradient is calculated via the gradient function of the Python package Numpy which uses central differences and forward/backwards difference for the boundary points. Therefore, we prop-

agate ΔB_{NV} into the vertical error bars ΔG_{z} of Fig. 3 for interior and boundary points separately. The error $\Delta C_{\mathrm{z,gen}}$ from Eq. (A2) translates into the horizontal error bars quadratically combined with the Δd_{NV}.

Appendix E: Pulse measurements

$T_{2\mathrm{E}}$ vs gradient

At every position in the gradient field the π- pulse time was first characterized with a standard Rabi measurement Fig. 11(a). A π-pulse is a resonant microwave pulse that inverts the population of the two level system. When applied around the X-axis, it can effectively flip the state from $|0\rangle$ to $|1\rangle$.

Fitting the Rabi oscillations with

$$A\sin(2\pi\nu_r t+\Phi)\exp(-\Gamma_{\mathrm{Rabi}}t)+C\,, \tag{E1}$$

we extract π- pulse durations of 55 ns (bright blue line in Fig. 11(a)). In Fig. 11 (b) we show the two different $T_{2\mathrm{E}}$ measurements for the readout pulse around the X and -X axis on the Bloch sphere. The two measurement are used to calculate the visibility as mentioned in the main text.

The horizontal error bars in Fig. 4 (main text) are calculated by measuring the gradient before the spin echo measurement and after the measurement was done. The first two datapoints in Fig. 4 (main text) do not have a horizontal error bars because we did not measure the gradient before and after the spin-echo sequence.

Modeling of the NV signal in presence of a mechanical drive

The mechanical oscillation, actuated by a piezo shaker driven at the mechanical resonance frequency, can be written as $x(t)=x_0\cos(\Omega_{\mathbf{m}}t+\phi_0)$, where $\Omega_{\mathbf{m}}, x_0$ and ϕ_0 are the resonator frequency, amplitude and phase respectively.

The semi-classical parametric spin-mechanics interaction Hamiltonian is:

$$\mathscr{H}^{\mathrm{int}}/\hbar=\pi\gamma_{\mathrm{NV}}G_{\mathrm{x}}x(t)\sigma_3, \tag{E2}$$

where $G_{\mathrm{x}}=\partial B_{\mathrm{NV}}/\partial x$ is the gradient - along the oscillator's motion direction (x) - of the magnetic field component (B_{NV}) parallel to the NV spin quantization axis. Here, σ_3 is the Pauli matrix.

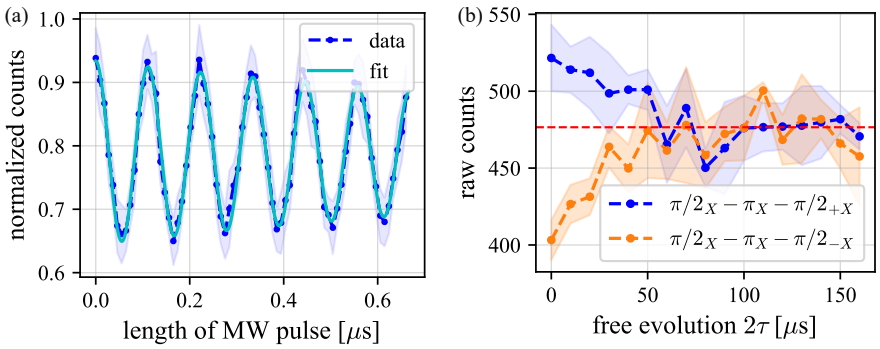

FIG. 11. (a) Rabi oscillations used to calibrate the π- and $\pi/2$-pulses. Usual π- pulse times of ca. 55 ns are extracted from the fit. The shaded area represents the standard deviation observed across multiple runs of the measurement. (b) Spin-echo measurements, for calculating visibility in the main text. The shaded area represents the standard deviation observed across multiple runs of the measurement. The red line indicates the baseline of the background counts.

Starting from the initial $|0\rangle$ state, the system evolves under the following spin echo pulse scheme: $[\pi/2 - \tau - \pi - \tau - \pi/2]$ where τ is the time between the pulses. The first $\pi/2$ pulse creates a superposition on the equator of the Bloch sphere which, up to a global phase, can be written as

$$|\Psi_0\rangle = \frac{1}{\sqrt{2}}\left(|0\rangle - i|1\rangle\right), \tag{E3}$$

in the frame rotating with the spin resonance frequency. At the end of the free evolution on the equatorial plane, the spin state can be written as

$$|\Psi_{2\tau}\rangle = \frac{1}{\sqrt{2}}\left(|0\rangle - ie^{-i\phi}|1\rangle\right), \tag{E4}$$

where the accumulated relative phase reads[18]

$$\phi(\tau) = \frac{2\pi\gamma_{\mathrm{NV}}G_x x_0}{\Omega_{\mathbf{m}}}\left[\sin(2\Omega_{\mathbf{m}}\tau + \phi_0) - 2\sin(\Omega_{\mathbf{m}}\tau + \phi_0) + \sin(\phi_0)\right]. \tag{E5}$$

Lastly, after the final read-out $\pi/2$ pulse, the probability to find the system in the $|0\rangle$ level is[15]

$$P_0 = |\langle\Psi_0|\Psi_{2\tau}\rangle|^2 = \frac{1}{2}\left(1 \mp \cos(\phi)\right), \tag{E6}$$

where the sign $\mp$ depends on whether the readout pulse is around the X or the $-X$ axis of the Bloch sphere. Assuming a uniformly distributed ϕ_0 during the pulse measurements, we get an average contrast:

$$\langle\cos(\phi(\tau))\rangle_{\phi_0} = J_0\left(\frac{4\pi\gamma_{\mathrm{NV}}G_x x_0}{\Omega_{\mathbf{m}}}(\cos(\Omega_{\mathbf{m}}\tau) - 1)\right). \tag{E7}$$

The visibility V_{echo}, as defined in the main text, reads:

$$V_{\text{echo}} = \frac{CJ_0\left(\frac{4\pi\gamma_{\text{NV}}G_x x_0}{\Omega_{\mathbf{m}}}(\cos(\Omega_{\mathbf{m}}\tau)-1)\right)}{2-C}\exp\left[-\left(\frac{2\tau}{T_{2\text{E}}}\right)^n\right], \tag{E8}$$

where we have added the exponential decay which accounts for the spin decoherence.

REFERENCES

[1] D. Rugar, R. Budakian, H. J. Mamin, and B. W. Chui, "Single spin detection by magnetic resonance force microscopy," Nature **430**, 329–332 (2004).

[2] M. D. LaHaye, J. Suh, P. M. Echternach, K. C. Schwab, and M. L. Roukes, "Nanomechanical measurements of a superconducting qubit," Nature **459**, 960–964 (2009).

[3] A. D. O'Connell, M. Hofheinz, M. Ansmann, R. C. Bialczak, M. Lenander, E. Lucero, M. Neeley, D. Sank, H. Wang, M. Weides, J. Wenner, J. M. Martinis, and A. N. Cleland, "Quantum ground state and single-phonon control of a mechanical resonator," Nature **464**, 697–703 (2010).

[4] J.-M. Pirkkalainen, S. U. Cho, J. Li, G. S. Paraoanu, P. J. Hakonen, and M. A. Sillanpää, "Hybrid circuit cavity quantum electrodynamics with a micromechanical resonator," Nature **494**, 211–215 (2013).

[5] S. Etaki, M. Poot, I. Mahboob, K. Onomitsu, H. Yamaguchi, and H. S. J. van der Zant, "Motion detection of a micromechanical resonator embedded in a d.c. squid," Nature Physics **4**, 785–788 (2008).

[6] M. Montinaro, G. Wüst, M. Munsch, Y. Fontana, E. Russo-Averchi, M. Heiss, A. Fontcuberta i Morral, R. J. Warburton, and M. Poggio, "Quantum dot opto-mechanics in a fully self-assembled nanowire," Nano Letters **14**, 4454–4460 (2014).

[7] D. A. Golter, T. Oo, M. Amezcua, K. A. Stewart, and H. Wang, "Optomechanical quantum control of a nitrogen-vacancy center in diamond," Phys. Rev. Lett. **116**, 143602 (2016).

[8] A. Bachtold, J. Moser, and M. I. Dykman, "Mesoscopic physics of nanomechanical systems," Rev. Mod. Phys. **94**, 045005 (2022).

[9] U. L. Andersen, J. S. Neergaard-Nielsen, P. van Loock, and A. Furusawa, "Hybrid discrete- and continuous-variable quantum information," Nature Physics **11**, 713–719 (2015).

[10] A. Eichler, "Ultra-high-q nanomechanical resonators for force sensing," Materials for Quantum Technology **2**, 043001 (2022).

[11] M. W. Doherty, N. B. Manson, P. Delaney, F. Jelezko, J. Wrachtrup, and L. C. Hollenberg, "The

nitrogen-vacancy colour centre in diamond," Physics Reports **528**, 1–45 (2013), the nitrogen-vacancy colour centre in diamond.

[12]A. Barfuss, J. Teissier, E. Neu, A. Nunnenkamp, and P. Maletinsky, "Strong mechanical driving of a single electron spin," Nature Physics **11**, 820–824 (2015).

[13]P. Ovartchaiyapong, K. W. Lee, B. A. Myers, and A. C. B. Jayich, "Dynamic strain-mediated coupling of a single diamond spin to a mechanical resonator," Nature Communications **5**, 4429 (2014).

[14]O. Arcizet, V. Jacques, A. Siria, P. Poncharal, P. Vincent, and S. Seidelin, "A single nitrogen-vacancy defect coupled to a nanomechanical oscillator," Nature Physics **7**, 879–883 (2011).

[15]S. Kolkowitz, A. C. Bleszynski Jayich, Q. P. Unterreithmeier, S. D. Bennett, P. Rabl, J. Harris, and M. D. Lukin, "Coherent sensing of a mechanical resonator with a single-spin qubit," Science **335**, 1603–1606 (2012).

[16]B. Pigeau, S. Rohr, L. Mercier de Lépinay, A. Gloppe, V. Jacques, and O. Arcizet, "Observation of a phononic mollow triplet in a multimode hybrid spin-nanomechanical system," Nature Communications **6**, 8603 (2015).

[17]T. Oeckinghaus, S. A. Momenzadeh, P. Scheiger, T. Shalomayeva, A. Finkler, D. Dasari, R. Stöhr, and J. Wrachtrup, "Spin–phonon interfaces in coupled nanomechanical cantilevers," Nano Letters **20**, 463–469 (2020), pMID: 31820999, https://doi.org/10.1021/acs.nanolett.9b04198.

[18]F. Fung, E. Rosenfeld, J. D. Schaefer, A. Kabcenell, J. Gieseler, T. X. Zhou, T. Madhavan, N. Aslam, A. Yacoby, and M. D. Lukin, "Toward programmable quantum processors based on spin qubits with mechanically mediated interactions and transport," Phys. Rev. Lett. **132**, 263602 (2024).

[19]S. Hong, M. S. Grinolds, P. Maletinsky, R. L. Walsworth, M. D. Lukin, and A. Yacoby, "Coherent, mechanical control of a single electronic spin," Nano Letters **12**, 3920–3924 (2012), pMID: 22800099, https://doi.org/10.1021/nl300775c.

[20]J. Gieseler, A. Kabcenell, E. Rosenfeld, J. D. Schaefer, A. Safira, M. J. A. Schuetz, C. Gonzalez-Ballestero, C. C. Rusconi, O. Romero-Isart, and M. D. Lukin, "Single-spin magnetomechanics with levitated micromagnets," Phys. Rev. Lett. **124**, 163604 (2020).

[21]P. Rabl, P. Cappellaro, M. V. G. Dutt, L. Jiang, J. R. Maze, and M. D. Lukin, "Strong magnetic coupling between an electronic spin qubit and a mechanical resonator," Phys. Rev. B **79**, 041302 (2009).

[22]S. D. Bennett, S. Kolkowitz, Q. P. Unterreithmeier, P. Rabl, A. C. Bleszynski Jayich, J. G. E. Harris, and M. D. Lukin, "Measuring mechanical motion with a single spin," New Journal of Physics **14**, 125004 (2012).

[23]P. Rabl, S. J. Kolkowitz, F. H. L. Koppens, J. G. E. Harris, P. Zoller, and M. D. Lukin, "A quantum spin transducer based on nanoelectromechanical resonator arrays," Nature Physics **6**, 602–608 (2010).

[24]E. Rosenfeld, R. Riedinger, J. Gieseler, M. Schuetz, and M. D. Lukin, "Efficient entanglement of spin qubits mediated by a hot mechanical oscillator," Phys. Rev. Lett. **126**, 250505 (2021).

[25]D. Lee, K. W. Lee, J. V. Cady, P. Ovartchaiyapong, and A. C. B. Jayich, "Topical review: spins and mechanics in diamond," Journal of Optics **19**, 033001 (2017).

[26]J. M. De Teresa, A. Fernández-Pacheco, R. Córdoba, L. Serrano-Ramón, S. Sangiao, and M. R. Ibarra, "Review of magnetic nanostructures grown by focused electron beam induced deposition (febid)," Journal of Physics D: Applied Physics **49**, 243003 (2016).

[27]QZabre Ltd, "Qzabre quantum scanning tips," (2025), accessed: 2025-08-07.

[28]G. Balasubramanian, I. Y. Chan, R. Kolesov, M. Al-Hmoud, J. Tisler, C. Shin, C. Kim, A. Wojcik, P. R. Hemmer, A. Krueger, T. Hanke, A. Leitenstorfer, R. Bratschitsch, F. Jelezko, and J. Wrachtrup, "Nanoscale imaging magnetometry with diamond spins under ambient conditions," Nature **455**, 648–651 (2008).

[29]P. Maletinsky, S. Hong, M. S. Grinolds, B. Hausmann, M. D. Lukin, R. L. Walsworth, M. Loncar, and A. Yacoby, "A robust scanning diamond sensor for nanoscale imaging with single nitrogen-vacancy centres," Nature nanotechnology **7**, 320–324 (2012).

[30]L. Rondin, J.-P. Tetienne, T. Hingant, J.-F. Roch, P. Maletinsky, and V. Jacques, "Magnetometry with nitrogen-vacancy defects in diamond," Reports on progress in physics **77**, 056503 (2014).

[31]A. Gruber, A. Dräbenstedt, C. Tietz, L. Fleury, J. Wrachtrup, and C. von Borczyskowski, "Scanning confocal optical microscopy and magnetic resonance on single defect centers," Science **276**, 2012–2014 (1997), https://www.science.org/doi/pdf/10.1126/science.276.5321.2012.

[32]A. Fernández-Pacheco, L. Skoric, J. M. De Teresa, J. Pablo-Navarro, M. Huth, and O. V. Dobrovolskiy, "Writing 3d nanomagnets using focused electron beams," Materials **13** (2020), 10.3390/ma13173774.

[33]J. M. Coey, *Magnetism and magnetic materials* (Cambridge university press, 2010).

[34]L. Žaper, P. Rickhaus, M. Wyss, B. Gross, K. Wagner, M. Poggio, and F. Braakman, "Scanning nitrogen-vacancy magnetometry of focused-electron-beam-deposited cobalt nanomagnets,"

ACS Applied Nano Materials **7**, 3854–3860 (2024), https://doi.org/10.1021/acsanm.3c05470.

[35]Y. Tsaturyan, A. Barg, E. S. Polzik, and A. Schliesser, "Ultracoherent nanomechanical resonators via soft clamping and dissipation dilution," Nature Nanotechnology **12**, 776–783 (2017).

[36]N. Bar-Gill, L. M. Pham, A. Jarmola, D. Budker, and R. L. Walsworth, "Solid-state electronic spin coherence time approaching one second," Nature communications **4**, 1743 (2013).

[37]L. Catalini, Y. Tsaturyan, and A. Schliesser, "Soft-clamped phononic dimers for mechanical sensing and transduction," Phys. Rev. Appl. **14**, 014041 (2020).

[38]M. Rossi, D. Mason, J. Chen, Y. Tsaturyan, and A. Schliesser, "Measurement-based quantum control of mechanical motion," Nature **563**, 53–58 (2018).

[39]D. Hälg, T. Gisler, Y. Tsaturyan, L. Catalini, U. Grob, M.-D. Krass, M. Héritier, H. Mattiat, A.-K. Thamm, R. Schirhagl, E. C. Langman, A. Schliesser, C. L. Degen, and A. Eichler, "Membrane-based scanning force microscopy," Phys. Rev. Appl. **15**, L021001 (2021).

[40]T. Gisler, D. Hälg, V. Dumont, S. Misra, L. Catalini, E. C. Langman, A. Schliesser, C. L. Degen, and A. Eichler, "Enhancing membrane-based scanning force microscopy through an optical cavity," Phys. Rev. Appl. **22**, 044001 (2024).

[41]N. Scozzaro, W. Ruchotzke, A. Belding, J. Cardellino, E. C. Blomberg, B. A. McCullian, V. P. Bhallamudi, D. V. Pelekhov, and P. C. Hammel, "Magnetic resonance force detection using a membrane resonator," Journal of Magnetic Resonance **271**, 15–20 (2016).

[42]J. G. Longenecker, H. J. Mamin, A. W. Senko, L. Chen, C. T. Rettner, D. Rugar, and J. A. Marohn, "High-gradient nanomagnets on cantilevers for sensitive detection of nuclear magnetic resonance," ACS Nano **6**, 9637–9645 (2012).

[43]S. K. de Boer, W. F. van Dorp, and J. T. M. De Hosson, "Charging effects during focused electron beam induced deposition of silicon oxide," Journal of Vacuum Science & Technology B **29** (2011).

[44]C. Magén, J. Pablo-Navarro, and J. M. De Teresa, "Focused-electron-beam engineering of 3d magnetic nanowires," Nanomaterials **11**, 402 (2021).

[45]J. M. Camacho and V. Sosa, "Alternative method to calculate the magnetic field of permanent magnets with azimuthal symmetry," Revista mexicana de física E **59**, 8–17 (2013).

[46]N. M. Israelsen, S. Kumar, M. Tawfieq, J. S. Neergaard-Nielsen, A. Huck, and U. L. Andersen, "Increasing the photon collection rate from a single nv center with a silver mirror," Journal of optics **16**, 114017 (2014).

[47]A. Vansteenkiste, J. Leliaert, M. Dvornik, M. Helsen, F. Garcia-Sanchez, and B. Van Waeyen-

berge, “The design and verification of mumax3,” AIP advances **4** (2014).

[48]L. Exl, S. Bance, F. Reichel, T. Schrefl, H. Peter Stimming, and N. J. Mauser, “Labonte’s method revisited: An effective steepest descent method for micromagnetic energy minimization,” Journal of Applied Physics **115** (2014).

[49]R. Cheenikundil and R. Hertel, “Switchable magnetic frustration in buckyball nanoarchitectures,” Applied Physics Letters **118** (2021).